Available online at www.sciencedirect.com
ScienceDirect
ELSEVIER
Journal of Catalysis 250 (2007) 1–11
JOURNAL OF CATALYSIS
www.elsevier.com/locate/jcat

# Catalytic behavior of hydrothermally synthesized $La_{0.5}Sr_{0.5}MnO_3$ single-crystal cubes in the oxidation of CO and $CH_4$

Fei Teng [a], Wei Han [b], Shuhui Liang [a], Buergen Gaugeu [a], Ruilong Zong [a], Yongfa Zhu [a,*]

[a] *Department of Chemistry, Tsinghua University, Beijing 100084, PR China*
[b] *State Key Laboratory of Catalysis, Dalian Institute of Chemical Physics, Dalian 116023, PR China*

Received 14 January 2007; revised 2 May 2007; accepted 6 May 2007

## Abstract

$La_{0.5}Sr_{0.5}MnO_3$ single-crystal cubes and nanoparticles were synthesized by hydrothermal and citrate routes, respectively. Their catalytic properties for low-temperature CO oxidation and high-temperature $CH_4$ combustion were evaluated, and the effects of crystal structure and morphology on the catalytic properties of the catalysts were investigated. The activity (220 °C) of the complete oxidation of CO over the single cubes was lower than that (190 °C) over the nanoparticles. After running at 600 °C for 48 h under the reaction conditions, the surface area of the nanoparticles decreased significantly, but the cubes nearly maintained their surface area. For $CH_4$ combustion, the $La_{0.5}Sr_{0.5}MnO_3$ cubes showed a higher activity ($T_{10} = 360\,°C$, $T_{10}$: the temperature at 10% conversion of $CH_4$) than the nanoparticles ($T_{10} = 440\,°C$). The different activities were attributed to their different crystal structures and morphologies.

*Keywords:* $La_{0.5}Sr_{0.5}MnO_3$; Single crystals; Cubes; Hydrothermal; Catalytic oxidation; CO; $CH_4$; Thermal stability

## 1. Introduction

Since the 1950s, manganites ($La_{1-x}A_xMnO_3$, A = Sr, Ba, Ca) have attracted much attention because of their unique physicochemical properties [1–4]. These solids, widely used as oxidation catalysts and as cathode materials in solid-oxide fuel cells, have been studied intensively [5,6]. They were prepared mainly using high-temperature ceramic, coprecipitation, citrate, and sol–gel routes [7–10]. The obtained materials are usually composed of assorted polycrystals with various exposed crystal planes that could exhibit the different catalytic activities. It is generally accepted that the crystal structure and morphology of the catalysts have a significant influence on activity [11–15]. Recently, Wang and Zhu reported that $SrCO_3$ nanowires showed higher activity for ethanol oxidation than the nanoparticles due to their different exposed lattice planes [14]. Besides, Zhou et al. reported that $CeO_2$ nanorods were more reactive for CO oxidation than the corresponding nanoparticles. They revealed that the predominantly exposed {001} and {110} crystal planes in $CeO_2$ nanorods were more reactive than the {111} crystal plane in the nanoparticles [15]. Therefore, designing or synthesizing highly reactive/selective catalysts has been an intriguing and challenging goal in heterogeneous catalysis [16,17]. Single crystals or well-defined superlattices of manganites are needed to elucidate their catalytic properties. Single-crystal materials have received much attention because of their different intriguing properties than those of polycrystal materials. Generally, single crystals of the manganites are grown using the flux and floating-zone melting methods [18–23]. However, these methods require high temperatures (>1000 °C) and complex operating procedures. Recently, $La_{0.5}A_{0.5}MnO_3$ (A = Ca, Sr, Ba) single crystals were synthesized under hydrothermal conditions and their magnetization properties were determined [24–29]. Nevertheless, to date, little work has been devoted to the study of the catalytic properties of these single-crystal cubes. It is desirable to research the catalytic properties of $La_{0.5}A_{0.5}MnO_3$ single-crystal cubes, which may differ from those of polycrystal nanoparticles.

In this work, $La_{0.5}Sr_{0.5}MnO_3$ single-crystal cubes were synthesized in one step by the hydrothermal method, and

---

* Corresponding author.
*E-mail address:* zhuyf@mail.tsinghua.edu.cn (Y. Zhu).

0021-9517/$ – see front matter © 2007 Elsevier Inc. All rights reserved.
doi:10.1016/j.jcat.2007.05.007

the effects of alkali concentration and hydrothermal temperature on the product were investigated. For comparison, $La_{0.5}Sr_{0.5}MnO_3$ nanoparticles were also prepared by the citrate method. The catalytic properties of the single-crystal cubes and the nanoparticles for the oxidation of CO and $CH_4$ were researched. The catalysts were characterized by X-ray diffraction (XRD), scanning electron microscopy (SEM), energy-dispersed spectra (EDS), transmission electron microscopy (TEM), high-resolution transmission electron microscopy (HRTEM), selected area electron diffraction (SAED), $N_2$ adsorption isotherm, laser Raman spectra (LRS), CO, $O_2$, $CH_4$ temperature-programmed desorption (TPD), and $H_2$ temperature-programmed reduction (TPR).

## 2. Experimental

### 2.1. Synthesis of $La_{0.5}Sr_{0.5}MnO_3$ single-crystal cubes

The synthesis of $La_{0.5}Sr_{0.5}MnO_3$ single-crystal cubes was carried out under hydrothermal conditions as described previously [28,29]. $KMnO_4$, $Mn(CH_3COO)_2{\cdot}4H_2O$, $Sr(CH_3COO)_2{\cdot}0.5H_2O$, and $La(CH_3COO)_3{\cdot}1.5H_2O$ were used as the starting materials, and KOH was used as the mineralization agent. All of the chemicals were analytical grade and used without purification. The molar ratios of La/Sr/Mn were kept at 0.5/0.5/1, based on the stoichiometric ratios of $La_{0.5}Sr_{0.5}MnO_3$. The molar ratio of $KMnO_4$ to Mn $(CH_3COO)_2$ was 3/7. Typically, the starting chemicals were dissolved in 40 mL of deionized water, and then 44.8 g of KOH was added to the solution under stirring. After 10 min of stirring, the mixture was poured into an autoclave (50 mL volume), and then subjected to hydrothermal treatment at 240 °C for 24 h. After cooling to room temperature, the solids were separated by centrifuging, washed with deionized water, and dried at 80 °C for 24 h. To investigate the effect of KOH concentration on the product, the concentration of KOH was varied from 20, 15, 10, and 5 $mol\,L^{-1}$.

### 2.2. Synthesis of $La_{0.5}Sr_{0.5}MnO_3$ nanoparticles

$La_{0.5}Sr_{0.5}MnO_3$ nanoparticles were prepared by the citrate method [9]. The solution was prepared by dissolving $Mn(CH_3COO)_2{\cdot}4H_2O$, $Sr(CH_3COO)_2{\cdot}0.5H_2O$, $La(CH_3COO)_3{\cdot}1.5H_2O$, and citric acid (CA) in deionized water, in which the molar ratios of La/Sr/Mn/CA were kept at 0.5/0.5/1/4. The resulting solution was evaporated at 80 °C and completely dried at 80 °C overnight in an oven. The spongy material thus obtained was crushed and calcined at 700 °C for 3 h under flowing air.

### 2.3. Characterization

The sample was characterized by XRD (Rigaku D/MAX-RB X-ray powder diffractometer), using graphite monochromatized $CuK_\alpha$ radiation ($\lambda = 0.154$ nm), operating at 40 kV and 50 mA. The patterns were scanned from 10° to 70° ($2\theta$) at a scanning rate of $1^\circ\,min^{-1}$. A nitrogen adsorption isotherm was performed at −196 °C on a Micromeritics ASAP2010 gas adsorption analyzer. The sample was degassed at 250 °C for 5 h before the measurement. Surface area was calculated by the BET method. The morphology of the catalyst was characterized by TEM using a JEOL 200CX microscope with an accelerating voltage of 200 kV. HRTEM (using a JEOL JEM-2010) was used to determine the surface structure of the sample. The powders were ultrasonically dispersed in ethanol and then deposited on a thin amorphous carbon film supported by a copper grid. Sample morphology and composition were also characterized by SEM, using a KYKY 2800 microscope equipped with a Link ISIS EDS analyzer with an acceleration voltage of 15 keV and a current of 1.2 nA. In the X-ray map recording, a current of 6.7 nA was used. LRS spectra were measured at room temperature using a Jobin Yvon/Atago-Bussan T-64000 triple spectrometer with a liquid nitrogen-cooled CCD detector. Acquisition time was between 800 and 1200 s. The green line ($\lambda = 514.5$ nm) of an $Ar^+$ laser was used to excite the Raman spectra, using a laser power of 20 mW on the sample. Measurements were made under the microscope, using a 90 microscopy objective; the laser spot size was around 1–2 μ. Raman measurements covered the range of 100–800 $cm^{-1}$. To obtain a high signal-to-noise ratio, the Raman spectrum was the average of 5 successive scans obtained at a spectral resolution of 2 $cm^{-1}$.

### 2.4. CO-TPD, $CH_4$-TPD, $O_2$-TPD, and $H_2$-TPR

The CO-TPD measurements were performed on a conventional CO-TPD instrument. To remove the pollutants adsorbed on the sample, 0.1 g of catalyst was loaded into a quartz reactor and heated in He flow at 250 °C for 2 h. Then the system was cooled to room temperature under the flowing He gas (40 $mL\,min^{-1}$). The sample was saturated with CO at room temperature for 0.5 h, and the excess adsorbates were removed by allowing the sample to remain in a He flow until no significant amount of adsorbates could be detected. The temperature was ramped to 600 °C at a linear heating rate of 20 $°C\,min^{-1}$. Mass spectrometry (MS) was used to monitor the variations of the $m/e$ ratio of CO (28) to $CO_2$ (44).

The $CH_4$- and $O_2$-TPD measurements were made using the same instruments used for CO-TPD. The catalyst was first pretreated in He atmosphere (30 $mL\,min^{-1}$) at 500 °C for 0.5 h, then cooled to 100 °C. Then the adsorption of gas was performed in a flow of 4 vol% $CH_4$ (balanced by He) or 20 vol% $O_2$ (balanced by He) for 30 min. In the flowing He gas, the catalyst bed was maintained at 100 °C for another 30 min to eliminate physically adsorbed $CH_4$ or $O_2$. Finally, the temperature was ramped to 600 °C for $CH_4$-TPD or 800 °C for $O_2$-TPD at a rate of 20 $°C\,min^{-1}$. The desorbed $CH_4$ or $O_2$ was analyzed using a gas chromatograph with a hydrogen flame ionization detector (GC–FID) for $CH_4$ or with a thermal conductivity detector (GC–TCD) for $O_2$.

$H_2$-TPR of the catalyst was conducted on a fixed-bed continuous-flow reactor–GC combination system. 20 mg of catalyst sample was used for each test. The sample was flushed by a purified argon stream, first at 400 °C for 30 min and then cooled to room temperature, followed by flushing with an He-carried 5 vol% $H_2$ gaseous mixture as reducing gas for starting the TPR test. The rate of temperature increase was 20 °C $min^{-1}$. Changes in the hydrogen signal were monitored using an online GC–TCD.

### 2.5. *Catalytic oxidation of CO and $CH_4$*

The oxidation of CO was carried out in a conventional flow system at atmospheric pressure. First, 0.1 g of catalyst was loaded into a quartz reactor (5 mm i.d.), with quartz beads packed at both ends of the catalyst bed. A thermocouple was placed in the catalyst bed to monitor the reaction temperature because CO oxidation is an exothermic reaction. Before each run, the catalyst was flushed with air (100 mL $min^{-1}$) at 600 °C for 1 h to remove adsorbed species from the surface, and then cooled to 30 °C. A gas mixture of 2 vol% CO and 98 vol% air was fed to the catalyst bed at a gas hourly space velocity (GHSV) of 12,000 $h^{-1}$. The inlet and outlet gas compositions were analyzed by an on-line gas chromatograph with a GDX-403 GC-column (1.5 m × 4 mm) at 100 °C and a hydrogen FID.

The combustion of $CH_4$ was conducted in a conventional flow system at atmospheric pressure. First, 0.1 g of catalyst was diluted with 0.1 g of quartz powder and loaded into a quartz reactor (5 mm i.d.) with quartz beads packed at both ends of the catalyst bed. The thermocouple was placed in the catalyst bed to monitor the reaction temperature, because $CH_4$ oxidation is an exothermic reaction. Before each run, the catalyst was flushed with air (100 mL $min^{-1}$) at 600 °C for 1 h to remove adsorbed species from the surface, then cooled to 200 °C. A gas mixture of 2 vol% $CH_4$ and 20 vol% $O_2$ (balanced with Ar) was fed into the catalyst bed at a GHSV of 100,000 $h^{-1}$. The inlet and outlet gas compositions were analyzed by online GC with a packed column of carbon molecular sieve (1.5 m × 4 mm) and a TCD.

To investigate the thermal stability of the catalyst, the reaction was run at 600 °C for 48 h under the reaction conditions. The conversion of $CH_4$ at 600 °C was measured every 4 h.

## 3. Results and discussion

### 3.1. *Hydrothermal synthesis of $La_{0.5}Sr_{0.5}MnO_3$ single-crystal cubes*

Fig. 1A gives the XRD patterns of the hydrothermally synthesized $La_{0.5}Sr_{0.5}MnO_3$ sample at 240 °C and 20 M KOH and the counterpart by the citrate method. No shift in the diffraction peaks can be observed for the samples, and all of the diffraction peaks can be well indexed to a pure perovskite structure with a high crystallinity. The XRD patterns of the hydrothermally synthesized $La_{0.5}Sr_{0.5}MnO_3$ sample can be indexed to a primitive cubic unit cell [space group *Pm3m*, $a = 0.3841(4)$ nm], in agreement with the lattice parameter of their bulk counterpart. To investigate their crystal structures, the wide-angle scanning was performed in the range of 65°–70°, as shown in Fig. 1B. A broadening of the diffraction peaks of the sample by the citrate method can be seen, compared with the hydrothermally synthesized sample. This indicates that the crystal size of the nanoparticle sample prepared by the citrate route is smaller than that of the sample prepared by the hydrothermal route. The average size of the nanocrystals is 20.7 nm, calculated using Scherrer's equation. Furthermore, although peak splitting was reduced to some extent due to the small crystal size of the nanoparticles, splitting of the {220} diffraction peak is still discernible in the nanoparticles. As shown in Fig. 1B (b), the {224} diffraction peak appears, consistent with the presence of a tetragonal crystal structure [space group *I4/mcm*, $a = 0.54806(3)$ nm, $c = 0.77206(6)$ nm]. The peak splitting is consistent with the presence of a tetragonal polymorph. The distorted structure might be due to the small size of the crystals and a large surface strain [30]; thus, it can be assumed that the nanoparticle sample may be a mixture structure of *I4/mcm* and *Pm3m*. Calculations using the XRD data reveal that the nanoparticle sample contains 60% cubic polymorph and 40% tetragonal polymorph. Woodward et al. previously reported that a $La_{0.5}Sr_{0.5}MnO_3$ sample prepared by a ceramic synthesis method comprised a mixture of cubic and tetragonal polymorphs [31]. This means that the $La_{0.5}Sr_{0.5}MnO_3$ samples

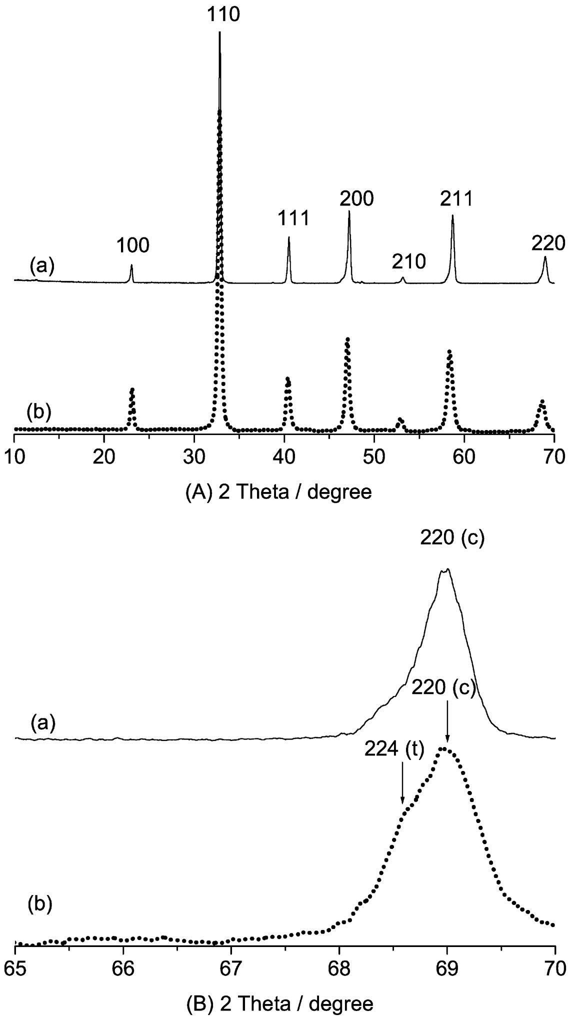

Fig. 1. The XRD patterns of the $La_{0.5}Sr_{0.5}MnO_3$ catalysts: (A) single-crystal cubes synthesized hydrothermally: 20 M KOH, 240 °C, 24 h; (B) nanoparticles prepared by the citrate route: calcined at 700 °C for 5 h.

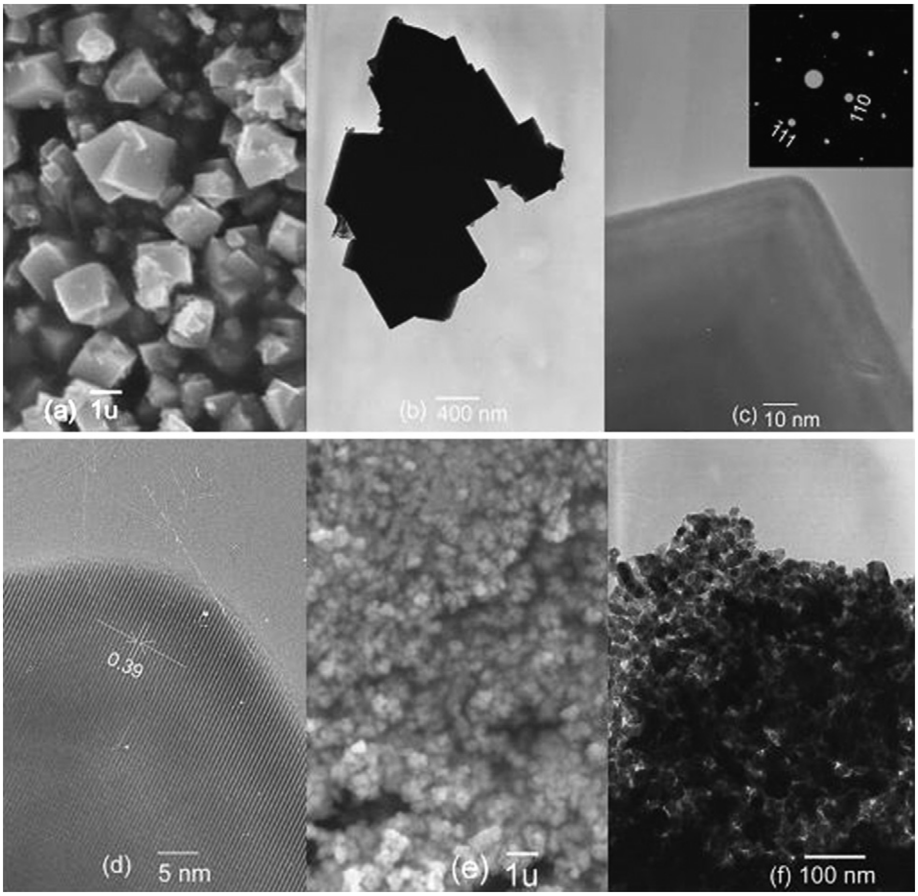

Fig. 2. SEM, TEM, HRTEM, and SAED images of the $La_{0.5}Sr_{0.5}MnO_3$ catalysts: (a, b, c, d) single-crystal cubes; (e, f) nanoparticles.

prepared by different methods have different crystal structures, as was further confirmed by LRS (as discussed later).

Furthermore, the morphologies of the $La_{0.5}Sr_{0.5}MnO_3$ samples were observed with SEM, TEM, and HRTEM. As shown in Figs. 2a and 2b, the hydrothermally synthesized $La_{0.5}Sr_{0.5}MnO_3$ sample consists of cubes with an average diameter of about 1.5 μ but a wide size distribution in the range of 0.1–2 μ. The sharp spots of in the SAED patterns (insert of Fig. 2c) confirm the single-crystal structure of the cubes. The absence of the extra reflections and/or the diffuse streaks suggests the presence of long-range ordering lattices. Fig. 2d shows that the surface of the cubes is clean and has no sheathed amorphous phase, whereas the clear lattice fringes confirm the high crystallinity and the single-crystalline nature. The interplanar spacing is calculated to be 0.39 nm, which is consistent with the {110} plane of a cubic $La_{0.5}Sr_{0.5}MnO_3$ crystal, indicating the preferred growth along the [100] direction. The EDS spectra (see Fig. S1 in Supplementary material) show that the compositions of the cubes are close to the stoichiometric ratios of $La_{0.5}Sr_{0.5}MnO_3$ (i.e., La:Sr:Mn = 25.59:24.44:49.11). On the other hand, the sample prepared by the citrate route comprises the nanoparticles (30–50 nm), as shown in Figs. 2e and 2f. It is clear that the synthesis method has a significant influence on the morphology of the product.

The control experiments were carried out to investigate the influence of alkali concentration and hydrothermal temperature on the formation of $La_{0.5}Sr_{0.5}MnO_3$ samples. At low concentrations of KOH (15, 10, and 5 M) or the low temperature (220 °C), the as-prepared products consisted of both cubes (0.1–2 μ) and nanowires (50–100 nm × 2 μ). Their XRD and SAED patterns confirm that the nanowires are $La(OH)_3$ and the cubes are perovskite (see Figs. S2 and S3 in Supplementary material). Further, the amount of perovskite phase decreased obviously with decreasing KOH concentration and temperature, but the amount of $La(OH)_3$ phase increased significantly. It is obvious that the KOH concentration and hydrothermal temperature have a significant influence on the phase compositions of the products, as has been reported by Spooren et al. [28] and Urban et al. [29]. It has been reported already that small changes in reaction conditions can affect the morphology of manganite [32]. At low alkalinity, the formation of $La(OH)_3$ crystals may be due to its low nucleation energy barrier. High alkalinity may provide a critical condition for the nucleation and crystallization of the manganites and is needed for the formation of the $La_{0.5}Sr_{0.5}MnO_3$ crystals, likely due to its high nucleation energy barrier. Chen et al. [33] have reported that the KOH concentration dominates the crystallization and formation of $Pr_{1-x}Ca_x MnO_3$. They also reported that the Mn-containing precursor is a critical factor in the formation of $La_{0.5}Sr_{0.5}MnO_3$ under hydrothermal conditions. The transformation from K-birnessite precursor to perovskite plays an important role in the preparation of mixed-valence manganese oxides, because the framework manganese of birnessite, usually (+2, +3, +4) or (+3 and +4), can easily transform to mixed-valence manganese in the products.

Some groups have reported the hydrothermal synthesis of the $La_{0.5}M_{0.5}MnO_3$ (M = Ca, Sr, Ba) "nanowires" [25–27, 34], but their TEM observation of the "nanowires" is puzzling. Before observation with TEM, the powders were first ultrasonically dispersed in ethanol and then deposited on a thin amorphous carbon film supported by copper grids. During preparation of the TEM sample, the large, heavy cubes can easily deposit on the bottom of the tubes while the light, small nanowires can be present stably in ethanol. As a result, only the light, small wires will be deposited on the Cu grid. In the $La(OH)_3$-containing sample, we only observed the "nanowires" without further intense shaking of the tube by hand after the ultrasonic stirring. If this sample was intensively shaken by hand further before taking drops of the sample, both the cubes and the nanowires were observed simultaneously (see Figs. S2 and S3 in Supplementary material). We believe that the TEM images represented the morphology of only a small part of the sample. Therefore, caution should be taken when observing the morphology of the sample with TEM. Although their XRD patterns of the "nanowires" can be indexed to the perovskite, a small portion of the $La(OH)_3$ crystals present in the product cannot be discerned by XRD. Therefore, we assume that the "nanowires" are actually $La(OH)_3$ crystals, not perovskite crystals. As a result, at low alkalinity or low temperature, the samples obtained were composed of both perovskite and $La(OH)_3$ crystals. Therefore, both high alkalinity and high temperature are necessary for the formation of single-phase $La_{0.5}Sr_{0.5}MnO_3$ crystals.

### 3.2. *Catalytic oxidation of CO over $La_{0.5}Sr_{0.5}MnO_3$ single-crystal cubes*

Fig. 3 gives the light-off curves of the CO oxidation over the $La_{0.5}Sr_{0.5}MnO_3$ catalysts. Here, $La_{0.5}Sr_{0.5}MnO_3$ cubes and nanoparticles are designated as C and P, respectively. The complete oxidation of CO was achieved at 220 °C over C and at 190 °C over P. The $La_{0.5}Sr_{0.5}MnO_3$ cubes clearly showed lower activity than the nanoparticles. The activity of the catalyst may be related to the number and distribution of the active sites, which are closely related to the textural properties and crystal structures of the catalysts [35]. The nanoparticles are smaller (30 nm) than the cubes (ca. 1.5 µ) (Fig. 2), and the BET surface area of the nanoparticles (20.56 $m^2\,g^{-1}$) is much larger than that of the cubes (3.71 $m^2\,g^{-1}$) (Table 1). The $La_{0.5}Sr_{0.5}MnO_3$ nanoparticles may supply more active sites than the cubes. Their different activities also may be related to their different fine crystal structures.

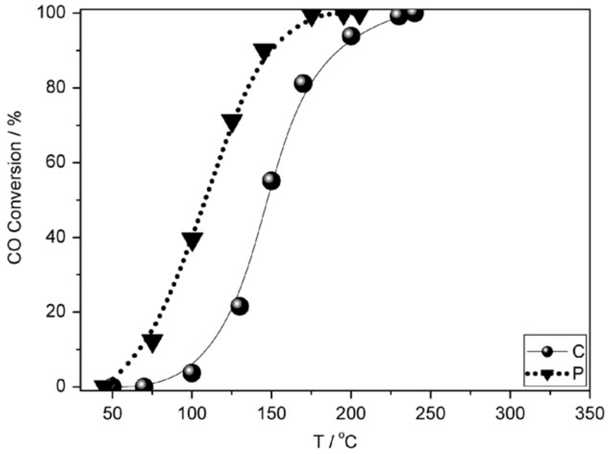

Fig. 3. The oxidation activities of CO over the $La_{0.5}Sr_{0.5}MnO_3$ catalysts: C, single-crystal cubes; P, nanoparticles.

Table 1
The reaction rate of CO at 120 °C and surface areas of the $La_{0.5}Sr_{0.5}MnO_3$ catalysts

| Sample | Preparation | SA[b] ($m^2\,g^{-1}$) | Reaction rate at 120 °C ($10^{-5}$ $mol\,h^{-1}\,m^{-2}$) |
|---|---|---|---|
| C[a] | Dried at 80 °C | 4.29 | 67.1 |
| P[a] | Calcined at 700 °C, 3 h | 20.56 | 91.5 |

[a] C and P, cubes and nanoparticles synthesized by the hydrothermal and citrate routes, respectively.

[b] SA, surface area by BET method.

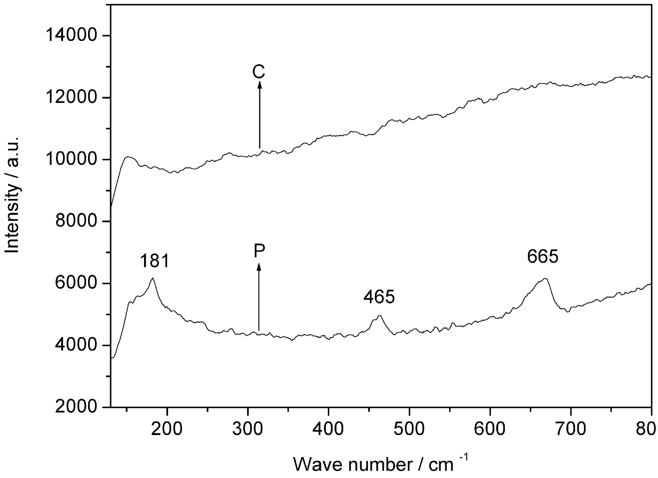

Fig. 4. LRS spectra of the $La_{0.5}Sr_{0.5}MnO_3$ catalysts.

To shed light on the relationship between crystal structure and catalyst activity, LRS scattering spectra of the $La_{0.5}Sr_{0.5}MnO_3$ samples were determined, as shown in Fig. 4. LRS spectroscopy is very sensitive not only to the structural phase transition, but also to the subtle changes in the local structure or the electronic states [36,37]. The LRS spectra of the doped $La_{1-x}A_xMnO_3$ crystals are composed of two parts, one part related to the distorted noncubic perovskite structure following the selection rules for first-order Raman scattering and the other part due mainly to the density of vibration states, classified as second-order Raman scattering. The Raman spectrum of the $La_{0.5}Sr_{0.5}MnO_3$ nanoparticles (P) shows three peaks in bands at 181, 463, and 665 $cm^{-1}$. The bands at 181 and 463 $cm^{-1}$ denote the polarization properties of $A_{1g}$ ($A_{1g}$, resulting from the motion of the oxygen ions) and $B_{1g}$ symmetry vibration modes involving mainly oxygen motions. Following the selection rules for first-order Raman scattering, these bands are related to the distorted noncubic perovskite structure (caused by ion substitution for *A*-site cations along certain directions and/or tilting of $MnO_6$ octahedral). Compared with the undoped $LaMnO_3$ compound, however, these bands are weaker [38]. Generally, the Jahn–Teller deformation of the $Mn^{3+}O_6$ octahedra lowers the local atomic site symmetry, and the new bands can be considered Jahn–Teller distortion-activated modes [39]. Because the partial substitution of Sr for La reduces the deviations from an ideal cubic structure, the presence of $Mn^{4+}$ generated by the doped Sr reduces the static Jahn–Teller distortion. The band at 665 $cm^{-1}$, which is much weaker than the bands of undoped $LaMnO_3$, is related mainly to a disordered perovskite structure [39]. The band correlates mainly with the Jahn–Teller effect or the density of states of the oxygen phonon, following the selection rules for second-order Raman scattering. Further considering the polarization properties of the corresponding Raman tensor components, the observed spectrum of the nanoparticles seems to be more consistent with a distorted $D_{4h}^5$ tetragonal structure [40,41]. For an average structure, the new Raman bands related to the local Jahn–Teller distortions will appear in the three intervals (about 180–300, 400–520, and 580–680 $cm^{-1}$), which seem to be typical for some previous Raman studies of perovskite structures in the near-cubic phase [42]. Therefore, it can be deduced that the nanoparticles share an average structure of cube (*Pm3m*) with tetragon (*I4/mcm*). Nevertheless, the $La_{0.5}Sr_{0.5}MnO_3$ cubes do not show the 181 and 463 $cm^{-1}$ bands (the first-order Raman scattering bands) that resulted from the smaller Jahn–Teller distortion of the ideal cubic structure. In an ideal cubic structure (*Pm3m*), all lattice sites have inversion symmetry, and the first-order Raman scattering is forbidden [42]. Moreover, the cube sample does not show the 665 $cm^{-1}$ band. The disappearance of the high-wavenumber broad peaks demonstrates that the cube sample has an idea cubic structure [42]. As a result, $MnO_6$ octahedron distortion by the $Mn^{3+}$ Jahn–Teller effect is less and the number of the oxygen vacancies in the single-crystal cubes is smaller than those in the nanoparticles. This may indicate that the single-crystal cubes have a more perfect cubic structure compared with the nanoparticles with an average structure. These results are consistent with those from XRD patterns. The different crystal structures can be expected to affect the adsorption of reacting molecules and the electron transfer between $Mn^{4+}$–O–$Mn^{3+}$.

$CO_2$-TPD and CO-TPD profiles after CO adsorption on $La_{0.5}Sr_{0.5}MnO_3$ catalyst were obtained to explore the distribution and number of the active sites. For the CO chemisorption on manganites, CO molecules would attach to the coordination sites of $MnO_6$ (unsaturated metal sites, $Mn^{3+}$), where some oxygen ligands are missing. It seems that CO and coordination sites of $MnO_6$ function as Lewis bases and Lewis acids, respectively. Chemisorption occurs by donation of 5$\sigma$ electrons in CO to Lewis acid sites of $MnO_6$. A significant portion of CO desorbed from the catalysts in the form of $CO_2$, and the total CO adsorption amount on the catalysts was consistent with the $CO_2$ and CO desorption amounts. The differences can be seen in the CO and $CO_2$ desorption profiles of the $La_{0.5}Sr_{0.5}MnO_3$ samples (Fig. 5). In the $CO_2$-TPD profiles of the $La_{0.5}Sr_{0.5}MnO_3$ catalysts (Fig. 5a), three $CO_2$ desorption peaks can be seen at 70, 145, and 345 °C for the nanoparticles, along with three peaks at 375, 425, and 560 °C for the single-crystal cubes. The CO-TPD profiles (Fig. 5b) show three CO desorption peaks at 170, 345, and 540 °C for the nanoparticles but only two peaks at 450 and 510 °C for the single-crystal cubes. Clearly, the intensity and the initial temperature of the $CO_2$ (CO) desorption peaks over the nanoparticles are stronger and lower than those over the single-crystal cubes, respectively. The quantitative analysis results given in Table 2 show that the total amount (194.3 µmol $g^{-1}$) of CO adsorption on $La_{0.5}Sr_{0.5}MnO_3$ nanoparticles is greater than that (137.0 µmol $g^{-1}$) on the single-crystal cubes, indicating that more active centers are located on the former than on the latter. Furthermore, at temperatures below 400 °C, the total adsorption amount of CO over the nanoparticles is larger than that over the cubes (161.6 vs 52.3 µmol $g^{-1}$), indicating that the nanoparticles could provide more active sites than the cubes at the lower temperatures. These results agree well with the order of the activity for CO oxidation. Nevertheless, above 400 °C, the total adsorption of CO over the cubes is higher than that over the nanoparticles (84.7 vs 32.7 µmol $g^{-1}$), suggesting that

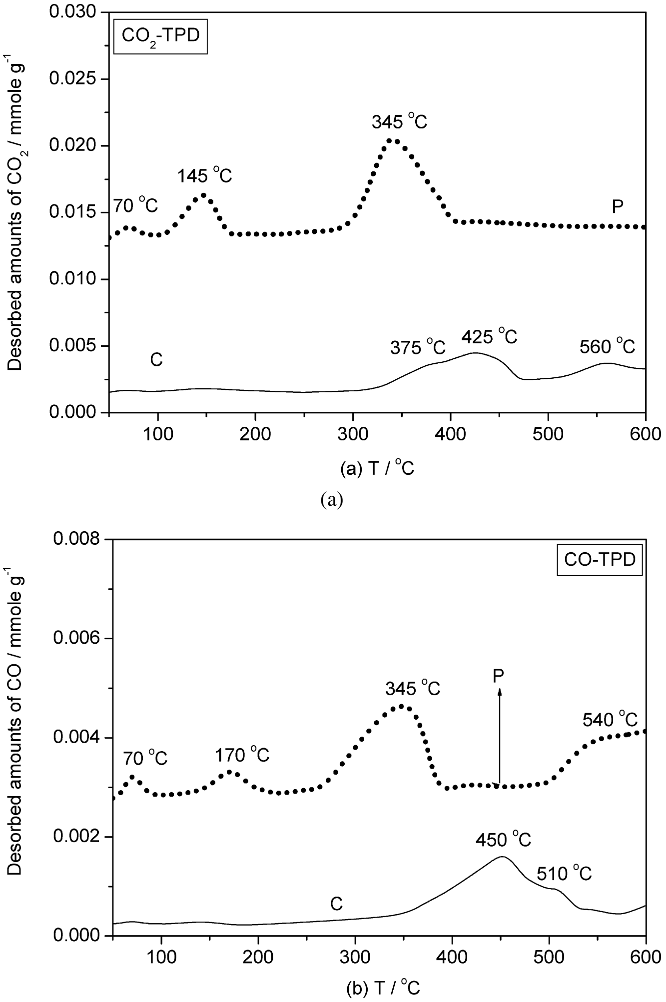

(a)

(b)

Fig. 5. $CO_2$-TPD (a) and CO-TPD (b) profiles of CO over the $La_{0.5}Sr_{0.5}MnO_3$ catalysts.

Table 2
The amounts of CO and $CO_2$ desorbed from the $La_{0.5}Sr_{0.5}MnO_3$ catalysts

| Sample | CO amount ($\mu mol\ g^{-1}/°C$) | | $CO_2$ amount ($\mu mol\ g^{-1}/°C$) | | Total amount of carbonaceous species ($\mu mol\ g^{-1}$) |
|---|---|---|---|---|---|
| | $T < 400$ | $400 < T < 600$ | $T < 400$ | $400 < T < 600$ | $T < 600$ |
| C | 15.6 | 40.5 | 36.7 | 44.2 | 137.0 |
| P | 56.3 | 32.7 | 105.3 | 0 | 194.3 |

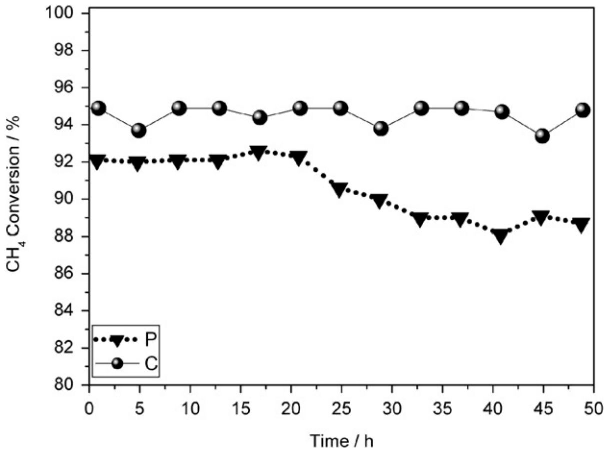

Fig. 6. The variations of $CH_4$ conversion over the $La_{0.5}Sr_{0.5}MnO_3$ catalysts with the duration at 600 °C under the reaction conditions: 2 vol% $CH_4$, 20 vol% $O_2$, GHSV = 100,000 $h^{-1}$.

the cubes have more active sites than the nanoparticles at higher temperatures. This may indicate that at high temperatures, the single cubes may have more active sites than the nanoparticles, which can be related to their different thermal stabilities. As a result, the cubes had lower activity than the nanoparticles for low-temperature CO oxidation.

Table 3
The reaction rates at 400 °C and the surface areas of the $La_{0.5}Sr_{0.5}MnO_3$ catalysts

| Sample | SA ($m^2\ g^{-1}$) | Reaction rate at 400 °C ($10^{-5}\ mol\ h^{-1}\ m^{-2}$) |
|---|---|---|
| C[a] | 3.73 | 21.7 |
| P[a] | 7.57 | 14.6 |

[a] After running for 48 h at 600 °C.

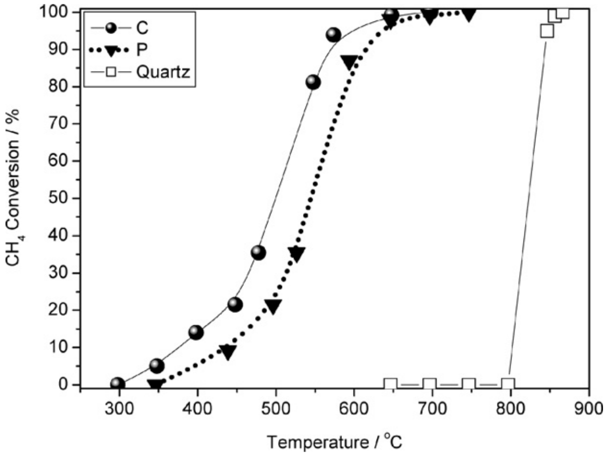

Fig. 7. Light-off curves of $CH_4$ over the $La_{0.5}Sr_{0.5}MnO_3$ catalysts after running at 600 °C for 48 h: 2 vol% $CH_4$, 20 vol% $O_2$, GHSV = 100,000 $h^{-1}$.

### 3.3. *Catalytic combustion of $CH_4$ over $La_{0.5}Sr_{0.5}MnO_3$ single-crystal cubes*

The combustion reaction of $CH_4$ was run at 600 °C for 48 h under the conditions of 2 vol% $CH_4$ and 20 vol% $O_2$. The $CH_4$ conversions at different durations of calcination are shown in Fig. 6. After running at 600 °C for 48 h, the conversion of $CH_4$ over the $La_{0.5}Sr_{0.5}MnO_3$ cubes was maintained (96%); but that over the nanoparticles decreased from 92 to 89%. A significant amount of water vapor was produced during this process, which would accelerate the sintering of the oxides under calcination at high temperatures. After the reaction was complete, the surface area of the cubes decreased slightly to 3.73 $m^2\ g^{-1}$ (or did not decrease), whereas that of the nanoparticles decreased significantly to 7.57 $m^2\ g^{-1}$ (see Table 3 and Fig. S4 in Supplementary material). It is obvious that the single-crystal cubes had higher thermal stability than the nanoparticles. Several pertinent factors should be considered. First, the surface-to-volume ratio of the cubes is larger than that of the nanoparticles, and thus there is a smaller driving force to sinter. Second, the contact area among the cubes may be small, which may also hinder sintering of the cubes. Finally, the perfect single-crystal structure may also contribute to the stability. Fig. 7 shows the light-off curves of $CH_4$ combustion over the $La_{0.5}Sr_{0.5}MnO_3$ catalysts after the reaction. Here the temperatures at 10 and 90% conversions of $CH_4$ are designated $T_{10}$ and $T_{90}$, respectively. The $La_{0.5}Sr_{0.5}MnO_3$ cubes showed higher activity ($T_{10} = 360\,°C$; $T_{90} = 570\,°C$) than the nanoparticles ($T_{10} = 440\,°C$; $T_{90} = 620\,°C$).

It is well known that at low conversions of methane, methane combustion is controlled mainly by surface catalytic reaction; at high conversions, the oxidation of methane usually includes surface reactions and free-radical reactions [43]. The free-radical reactions are more dependent on mass transfer than on the surface reactions. Before the gases react on the solid surface, gas diffusion from bulk gases to the solid surface occurs. Because the surface reaction is relatively fast, the influence of mass transfer from the gas bulk to the catalyst surface on the reaction should not be ignored. The balance between surface reaction and mass transfer may be affected by various factors, including intrinsic activity, particle sizes, porosity and concentration of catalyst. The catalyst's large surface area is beneficial to mass transfer, because it may favor the adsorption of more gases on the solid surface [43]. As a result, the $T_{10}$ difference of these samples is 80 °C, which is higher than their $T_{90}$ difference

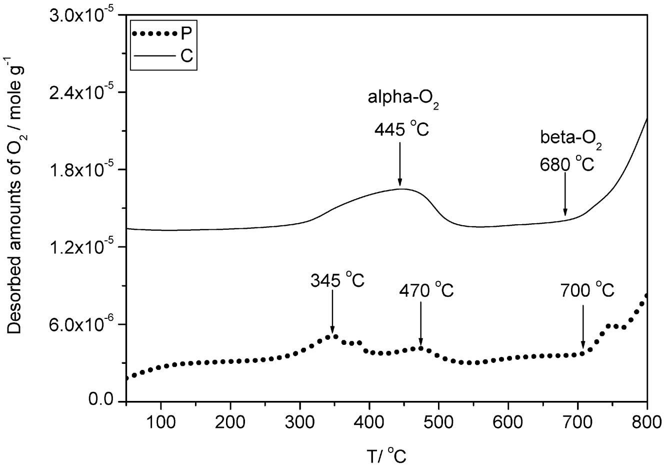

Fig. 8. $O_2$-TPD profiles from the $La_{0.5}Sr_{0.5}MnO_3$ catalysts.

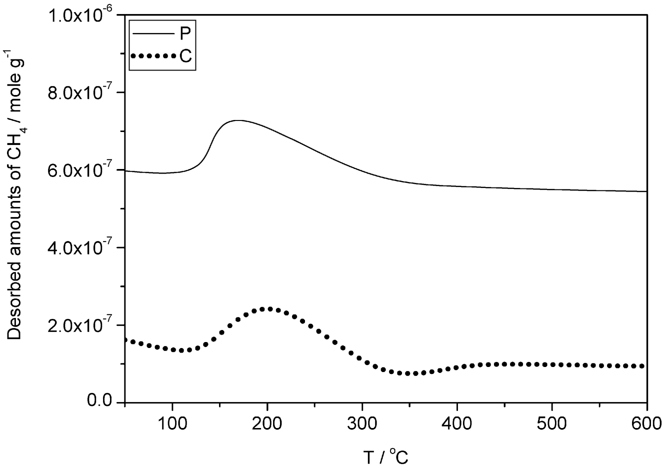

Fig. 9. $CH_4$-TPD profiles from the $La_{0.5}Sr_{0.5}MnO_3$ catalysts.

Table 4
The desorbed amounts of $O_2$ and $CH_4$ from the $La_{0.5}Sr_{0.5}MnO_3$ catalysts

| Catalyst | Desorbed amount of $O_2$ (μmol $g^{-1}$) | | Desorbed amount of $CH_4$ (μmol $g^{-1}$) | |
|---|---|---|---|---|
| | α-Oxygen <700 °C | β-Oxygen 700–800 °C | <400 °C | >400 °C |
| C | 65.8 | 76.2 | 0.31 | 0 |
| P | 38.2 | 70.5 | 0.29 | 0 |

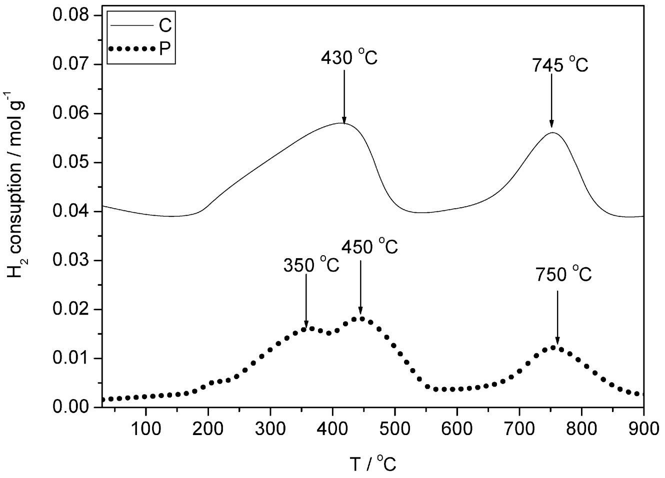

Fig. 10. $H_2$-TPR profiles of the $La_{0.5}Sr_{0.5}MnO_3$ catalysts.

(50 °C). Considering the different BET areas of the catalysts, the intrinsic activity of the catalyst was of main concern.

$CH_4$- and $O_2$-TPD were performed to investigate the adsorption of the reacting species. Fig. 8 gives the $O_2$-TPD profiles over the $La_{0.5}Sr_{0.5}MnO_3$ catalysts. It is well known that the desorption peaks of oxygen at lower temperatures result from the oxygen adsorbed on the catalyst surface (designated $\alpha$-oxygen), and the desorbed amount of $\alpha$-oxygen can be referred to surface oxygen vacancies. It is also well known that the desorption peaks of oxygen at high temperatures can be referred to the reduction of Mn ion (designated $\beta$-oxygen) [44]. As seen in Fig. 8, $\alpha$-$O_2$ desorbed at 250–550 °C, and $\beta$-$O_2$ desorbed above 700 °C. The adsorption amounts of $\alpha$- and $\beta$-$O_2$ from $La_{0.5}Sr_{0.5}MnO_3$ cubes were 65.8 and 76.2 μmol $g^{-1}$, respectively, larger than those from the nanoparticles (38.2 and 65.7 μmol $g^{-1}$). Fig. 9 shows the $CH_4$-TPD profiles over the $La_{0.5}Sr_{0.5}MnO_3$ catalysts. As shown, $CH_4$ desorbed at 100–400 °C, and nearly no desorption of $CH_4$ occurred above 400 °C. The adsorption amounts of $CH_4$ over both samples were nearly same (0.31 vs 0.29 μmol $g^{-1}$).

Table 4 clearly shows that $O_2$ desorption amount from both catalysts was far larger than that of $CH_4$ at 350–550 °C, where catalytic combustion occurred. This indicates that the combustion of $CH_4$ might proceed with the surface reaction between the gaseous $CH_4$ and the adsorbed or/and bulk oxygen. Marchetti and Forni [45] concluded that the oxidation of methane over $SrFeO_3$ occurs by means of the oxygen from the catalyst, even in the presence of gaseous oxygen. Therefore, the existence of oxygen in the vacancies of $La_{0.5}Sr_{0.5}MnO_3$ phases is of great importance to the process, and the catalyst's oxidation ability increases with increasing lattice oxygen mobility. Compared with the undoped $LaMnO_3$ compound, cationic vacancies are suppressed and anionic vacancies are created by the substitution of 50% La by Sr, so that the $\beta$-peak decreases noticeably and the $\alpha$-peak appears. It can be assumed that $La_{0.5}Sr_{0.5}MnO_3$ nanoparticles appear as the most active catalyst at low temperatures, because they have more adsorbed oxygen on their surfaces. In contrast, at high temperatures, when the lattice oxygen becomes available, $La_{0.5}Sr_{0.5}MnO_3$ cubes showed the most catalytic activity, because of the fast transfer rate of oxygen excess in its structure [46].

$H_2$-TPR profiles of the $La_{0.5}Sr_{0.5}MnO_3$ catalysts were obtained to investigate the relative reducibility of the catalyst, as shown in Fig. 10 and Table 5. For the $La_{0.5}Sr_{0.5}MnO_3$ nanoparticles, $H_2$-TPR peaks were observed at 350, 450, and 750 °C; for the $La_{0.5}Sr_{0.5}MnO_3$ cubes, two reduction peaks were observed at 430 and 745 °C. Because both $La^{3+}$ and $Sr^{2+}$ are nonreducible under the $H_2$-TPR condition, the reduction peaks should result from the reduction of Mn. All of these profiles showed two clear reduction regions, at 150–550 and 550–900 °C. The peak at 380–530 °C shifted slowly to lower temperature. As a result, the second reduction step

Table 5
The consumed amounts of $H_2$ of the $La_{0.5}Sr_{0.5}MnO_3$ catalysts

| Catalyst | $H_2$ amount of (mol g$^{-1}$) | $H_2$ amount of (mol g$^{-1}$) |
|---|---|---|
| | <600 °C | >600 °C |
| C | 3.23 | 1.33 |
| P | 3.21 | 1.31 |

was strongly activated [47], which was assigned to the reduction of $Mn^{3+}$ to $Mn^{2+}$. Conceivably, the partial substitution of $Sr^{2+}$ for $La^{3+}$ would result in increased concentrations of both $Mn^{4+}$ and oxygen vacancies, leading to increased reducibility of the catalyst. The small peak (or shoulder) at slightly lower temperatures (about 200 °C) can be assigned to removal of the nonstoichiometric excess oxygen accommodated within the lattice [47]. Thus, the $H_2$-TPR peaks at 350 °C can be attributed to the reduction of $Mn^{4+}$ to $Mn^{3+}$ and/or to a single electron reduction of $Mn^{3+}$ located in a highly coordination-unsaturated microenvironment. The 450 °C peaks may have resulted from a single-electron reduction of $Mn^{3+}$ located in a coordination-unsaturated microenvironment. Vogel et al. reported that first $LaMnO_{3.13}$ was reduced to a stoichiometric compound at 550 °C, and then the latter compound was reduced to manganese(II) oxide by one electron at 1050 °C [47]. The partially reduced $La_{0.5}Sr_{0.5}MnO_{3-\delta}$ intermediate thus produced still preserved the perovskite phase structure as a whole. The peak at about 745 °C most likely corresponded to the reduction of the remaining $Mn^{3+}$ to $Mn^{2+}$, leading to the breakdown of the perovskite phase and the formation of the discrete oxide phases ($La_2O_3$, SrO, and MnO). The color of the samples, initially black, became gray after reduction at 930 °C, suggesting that these new phases were present. The stability of $Mn^{4+}$ is probably the most important parameter, but excess of oxygen should also be taken into account. These two samples consumed similar amounts of $H_2$, but the center positions of their reduction peaks for the cubes shifted to slightly lower temperatures than those of the nanoparticles, indicating the easy reducibility of the cubes. This may be related to their cubic structure, in which the bond angle of $Mn^{3+}$–O–$Mn^{4+}$ is 180°, favoring electron transfer [48]. However, for the nanoparticles with average structure containing distorted tetragon structure does not.

### 3.4. Different catalytic mechanisms of CO and $CH_4$ over $La_{0.5}Sr_{0.5}MnO_3$ catalysts

Methane combustion on metal oxides is known to follow a redox mechanism [49]. In the oxidation–reduction model, the limiting step is a reaction occurring between strongly bound surface oxygen from the oxide lattice and weakly adsorbed methane molecules. The pairs of $Mn^{4+}$–$Mn^{3+}$ on the surface or near the surface may have a significant effect on activity. The high percentage of $Mn^{4+}$–$Mn^{3+}$ pairs favors the surface reaction. Such pairs might be particularly favorable for adsorption–desorption flip-flops when remaining isolated from neighboring pairs. In such a case, charge transfer from one ion to its partner and vice versa should be easy, because there is no reason for the electron to remain localized in one or the other cation. Another contribution to the catalytic activity that also might be related to the unusual $Mn^{3+}$ oxidation state is the occupancy of $e_g$ and $t_{2g}$ orbitals. Previous studies on the influence of B cations on the catalytic activity of $ABO_3$ for the CO oxidation have shown that the maximum activity is attained for an occupation of the $e_g$ levels of less than one electron, while at the same time the $t_{2g}$ electrons are half-filled or totally filled [50].

Because the oxidation of methane occurs by means of the surface oxygen (adsorbed or lattice oxygen) from the catalyst, even in the presence of gaseous oxygen, [51] the existence of oxygen in the vacancies of $La_{0.5}Sr_{0.5}MnO_3$ phases is vitally important to the process. The gaseous oxygen replaces the spent oxygen from the bulk through a Mars–Van Krevelen mechanism. The rate of the oxidation/reduction cycle and the oxygen desorption capacity of catalysts are also important for low-temperature oxidation of $CH_4$, as demonstrated by Machida et al. [52]. The defective and cation-deficient lattice, as well as the unstable oxidation states of manganese ($Mn^{3+}$/$Mn^{4+}$) resulting in an oxygen excess, have been considered the main origins of the $LaMnO_{3+\lambda}$ activity [53]. The catalytic activity of binary perovskites can be further enhanced by the partial substitution of Ba for La, which can induce nonstoichiometric oxygen. This may have two consequences. First, a large proportion of metal ions in the unstable oxidation state may be formed. Using X-ray absorption near-edge spectroscopy, Spooren et al. confirmed an average manganese oxidation state in $La_{0.5}Sr_{0.5}MnO_3$ of 3.5 [24]. Second, the oxygen mobility is greatly enhanced, related to a structural effect of single-crystal cubes. At $t$ (tolerance factor) $= 1$, the ideal perovskite has a cubic structure, with a $Mn^{3+}$–O–$Mn^{4+}$ angle of 180° and no tilt of the octahedral. These properties favor electron transfer, resulting in good reactivity. In fact, in the case of an electron-hopping mechanism in a perovskite, $Mn^{3+}$–O–$Mn^{4+}$ bond angles close to 180° optimize the electron-transfer process. With respect to a tetragonal structure, the cubic surface should make the hopping process easier, because possible carriers' localization phenomena should be highly minimized [54]. In manganese-containing perovskite, the presence of Mn ions with different oxidation states is critically important to the transport properties and the catalytic activity. It has been shown that in the simultaneous presence of $Mn^{3+}$ and $Mn^{4+}$, electron hopping between those two ions with intervening oxygen is the basic conduction mechanism. Hopping is favored at a 180° $Mn^{3+}$–O–$Mn^{4+}$ angle in the cubic structure [48].

Concerning the oxidation reaction, it has been clarified that the surface oxygen (bulk and adsorbed oxygen) play the most important roles [53,55]. The rate of methane combustion was low below 400 °C and then grew very fast above 400 °C, suggesting that two kinds of oxygen are involved in the reaction. The surface-adsorbed oxygen is active at low temperatures and its coverage decreases with increasing temperature, whereas the bulk oxygen becomes available at high temperatures. These findings have been confirmed by XPS spectra [51]. Thus, the adsorbed oxygen particulates are available at low temperatures, and the bulk oxygen species are available at high temperatures.

For the low-temperature oxidation of CO, oxygen adsorption occurs mainly above 300 °C, due to the bulk or gaseous oxygen reacting with the CO species. Indeed, the substitution of $Sr^{2+}$ for $La^{3+}$ creates anionic vacancies that improve the catalytic activity. The oxygen exchange reaction occurs at 200–300 °C, where adsorbed oxygen related to the anionic vacancies controls perovskite reactivity. This finding confirms that the oxygen-exchange reaction is a suprafacial reaction, tightly connected to the presence of anionic vacancies on the catalyst surface. The suprafacial mechanism is usually active when oxygen mobility is low [56]. Considering the slow diffusion of bulk oxygen at low temperatures (below 400 °C), the reacted oxygen may be mainly gaseous oxygen. It is conceivable that the CO oxidation reaction may proceed via the interaction between the adsorbed CO and the gaseous oxygen.

For the high-temperature oxidation of $CH_4$, adsorption of $CH_4$ on the catalyst is much weaker than that of oxygen, and $CH_4$ does not adsorb above 400 °C. Furthermore, the catalyst showed relatively low activity below 400 °C, with $CH_4$ oxidation occurring mainly above 400 °C. Considering the interplay between the exothermicity of the adsorption process and the kinetics of the catalytic reaction [54], it can be seen that the adsorption of the interacting molecules is favored at lower temperatures, whereas the mobility of bulk oxygen is enhanced at higher temperatures [54]. Because bulk oxygen is fairly mobile above 400 °C, the contribution of bulk oxygen to the reaction may become more relevant. Indeed, it is well known [56] that the intrafacial mechanism (active above 400 °C) is preferred when high ionic mobility favors the participation of bulk oxygen. In a steady-state operation, bulk diffusion of oxygen may speed up the reaction at high temperatures; however, in that case there may be specific sites at which oxygen is activated and built into the lattice, from which it diffuses to other specific sites via the bulk where the oxygen provided through diffusion interacts with CO or $CH_4$. This principle has been claimed for many Mars–Van Krevelen catalysts [51]. We can tentatively assume that bulk oxygen plays the most important role in $CH_4$ oxidation, and that the $CH_4$ oxidation reaction may proceed mainly through the interaction between the gaseous $CH_4$ and the adsorbed oxygen and/or bulk oxygen. A more powerful proof of this awaits further research.

## 4. Conclusion

High alkalinity may provide a critical condition for the nucleation and crystallization of manganites and is necessary for the formation of $La_{0.5}Sr_{0.5}MnO_3$ single-crystal cubes. The single-crystal cubes showed higher catalytic activity (220 °C) than the nanoparticles (190 °C) for the oxidation of CO. Compared with $La_{0.5}Sr_{0.5}MnO_3$ nanoparticles, the single-crystal cubes showed higher thermal stability after running at 600 °C for 48 h under the reaction conditions. For $CH_4$ combustion, the $La_{0.5}Sr_{0.5}MnO_3$ cubes showed higher activity ($T_{10} = 360\,°C$) than the nanoparticles ($T_{10} = 440\,°C$). The different activities were attributed to their differing crystal structures and morphologies. It was assumed that for the low-temperature oxidation, the CO oxidation reaction may proceed via the interaction between the adsorbed CO and the gaseous oxygen; for the high-temperature oxidation of $CH_4$, bulk oxygen played the most important role in $CH_4$ oxidation, and the $CH_4$ oxidation reaction might proceed mainly by the interaction between the gaseous $CH_4$ and the adsorbed oxygen and/or bulk oxygen.

## Acknowledgments

This work was supported by the Chinese National Science Foundation (Grants 20433010 and 20571047).

## Supplementary material

The online version of this article contains additional supplementary material.

Please visit DOI:10.1016/j.jcat.2007.05.007.

## References

[1] W.F. Libby, Science 171 (1971) 449.
[2] C.D.B. Meadow, Nature 226 (1970) 8472.
[3] W. Libby, Science 171 (1971) 4992.
[4] L.A. Pederson, W. Libby, Science 176 (1972) 13552.
[5] T. Seiyama, Catal. Rev. 34 (1992) 281.
[6] N. Minh, J. Am. Ceram. Soc. 76 (1993) 563.
[7] R.J.H. Voorhoeve, J.P. Remeika, L.E. Trimble, Ann. NY Acad. Sci. 272 (1976) 3.
[8] T. Nakamura, M. Misono, T. Uchijima, Y. Yoneda, Nippon Kagaku Kaishi (1978) 1462.
[9] M.S.G. Baythoun, F.R. Sale, J. Mater. Sci. 17 (1982) 2757.
[10] S. Bilger, E. Syskakis, A. Naoumidia, H. Nickel, J. Am. Ceram. Soc. 75 (1992) 964.
[11] S. Jaenicke, G.K. Chuah, B. Bunsenges, Phys. Chem. 96 (1992) 1.
[12] Y.M. Lin, S.B. Cronin, J.Y. Ying, M.S. Dresselhaus, J.P. Heremans, Appl. Phys. Lett. 76 (2000) 3944.
[13] J.C. Johnson, H.Q. Yan, R.D. Schaller, L.H. Haber, R.J. Saykally, P.D. Yang, J. Phys. Chem. B 105 (2001) 11387.
[14] L. Wang, Y.F. Zhu, J. Phys. Chem. B 109 (2005) 5118.
[15] K.B. Zhou, X. Wang, X.M. Sun, Q. Peng, Y.D. Li, J. Catal. 229 (2005) 206.
[16] T. Bell, Science 299 (2003) 1668.
[17] H.H. Kung, M.C. Kung, Appl. Catal. A 246 (2003) 193.
[18] K.N. Clausen, W. Hayes, D.A. Keen, R.M. Kusters, R.L.J. Singleton, J. Phys. Condens. Matter 1 (1989) 2721.
[19] Y.X. Jia, L. Khazeni, K. Lu, V.H. Crespi, A. Zettl, M.L. Cohen, Phys. Rev. B 52 (1995) 9147.
[20] G.D. Revcolevschi, Adv. Mater. 5 (1993) 657.
[21] M.F. Hennion, J. Moussa, L.R.C. Pinsard, A. Revcolevschi, Phys. Rev. B 56 (1997) R497.
[22] Y. Asamitsu, Y. Moritomo, T. Tomioka, Y.T. Arima, Nature 373 (1995) 407.
[23] M.R. Lees, J.D.M. Barratt, G. Paul, Phys. Rev. B 52 (1995) 14303.
[24] J. Spooren, R.I. Walton, F. Millange, J. Mater. Chem. 15 (2005) 1542.
[25] D. Zhu, H. Zhu, Y. Zhang, Appl. Phys. Lett. 80 (2002) 1634.
[26] D. Zhu, H. Zhu, Y. Zhang, J. Cryst. Growth 249 (2003) 172.
[27] J. Liu, H. Wang, M. Zhu, B. Wang, H. Yan, Mater. Res. Bull. 38 (2003) 817.
[28] J. Spooren, A. Rumplecker, F. Millange, R.I. Walton, Chem. Mater. 15 (2003) 1401.
[29] J.J. Urban, L. Ouyang, M.H. Jo, D.S. Wang, H. Park, Nano Lett. 4 (8) (2004) 1547.
[30] R. Bindu, S.K. Pandey, A. Kumar, S. Khalid, A.V. Pimpale, J. Phys. Condens. Matter 17 (2005) 6393.
[31] P.M. Woodward, T. Vogt, D.E. Cox, A. Arulraj, C.N.R. Rao, P. Karen, A.K. Chettham, Chem. Mater. 10 (1998) 3652.
[32] W. Boujelben, M. Ellouze, A. Cheikh-Rouhou, J. Pierre, J.C. Joubert, J. Solid State Chem. 165 (2002) 375.

[33] Y. Chen, H.M. Yuan, G. Tian, G.H. Zhang, S.H. Feng, J. Solid State Chem. 180 (2007) 167.
[34] T. Zhang, C.G. Jin, T. Qian, X.L. Lu, J.M. Bai, X.G. Li, J. Mater. Chem. 14 (2004) 2787.
[35] Y. Zhu, J. Shi, Z. Zhang, C. Zhang, X. Zhang, Anal. Chem. 74 (2002) 120.
[36] R. Gupta, A.K. Sood, R. Mahesh, C.N.R. Rao, Phys. Rev. B 54 (1996) 14899.
[37] V.B. Podobedov, A. Weber, D.B. Romero, J.P. Rice, H.D. Drew, Bull. Am. Phys. Soc. 42 (1997) 341.
[38] V.B. Podobedov, A. Weber, D.B. Romero, J.P. Rice, H.D. Drew, Phys. Rev. 58 (1998) 43.
[39] J.B. Goodenough, A. Wold, R.J. Arnott, N. Menyuk, Phys. Rev. 124 (1961) 373.
[40] N.I. Milko, V.A. Miroslav, J. Raman Spectrosc. 32 (2001) 805.
[41] V.B. Podobedov, A. Weber, D.B. Romero, J.P. Rice, H.D. Drew, Solid State Commun. 105 (1998) 589.
[42] E. Liarokapis, T. Leventouri, D. Lampakis, Phys. Rev. B 60 (1999) 12758.
[43] E.M. Johansson, K.M.J. Danielsson, E. Pocoroba, E.D. Haralson, S.G. Jåräs, Appl. Catal. A 182 (1999) 199.
[44] T. Nitadori, S. Kurihara, M. Misono, J. Catal. 98 (1986) 221.
[45] L. Marchetti, L. Forni, Appl. Catal. B 15 (1998) 179.
[46] T. Nitadori, S. Kurihara, M. Misono, J. Catal. 98 (1986) 221.
[47] E.M. Vogel, D.W. Johnson Jr., P.K. Gallagher, J. Am. Ceram. Soc. 60 (1977) 31.
[48] D.K. Chakrabarty, D.Y. Rao, React. Kinet. Catal. Lett. 33 (1987) 131.
[49] H. Arai, T. Yamada, K. Eguchi, T. Seiyama, Appl. Catal. 26 (1986) 265.
[50] V.C. Belessi, A.K. Ladavos, P.J. Pomonis, Appl. Catal. B 31 (2001) 183.
[51] L. Marchetti, L. Forni, Appl. Catal. B 15 (1998) 179.
[52] M. Machida, K. Eguchi, H. Arai, J. Catal. 123 (1990) 477.
[53] Kosima, H. Adachi, I. Yasumori, Surf. Sci. 130 (1983) 50.
[54] L. Malavasi, C. Tealdi, G. Flor, G. Chiodelli, V. Cervetto, A. Montenero, M. Borella, Sens. Actuators B 105 (2005) 407.
[55] K.S. Chan, J. Ma, S. Jaenicke, G.K. Chuan, Appl. Catal. A 107 (1994) 201.
[56] N. Yamazoe, Y. Teraoka, Catal. Today 8 (1990) 175.